

PENNSTATE



## ASTRONOMY AND ASTROPHYSICS

**Hard X-Ray Spectra of Broad-Line Radio Galaxies from the Rossi X-Ray Timing Explorer**

Michael Eracleous & Rita Sambruna

Department of Astronomy and Astrophysics, The Pennsylvania State University,

525 Davey Laboratory, University Park, PA 16802

e-mail: [mce@astro.psu.edu](mailto:mce@astro.psu.edu), [sambruna@astro.psu.edu](mailto:sambruna@astro.psu.edu)

and

Richard F. Mushotzky

NASA/GSFC, Code 662, Greenbelt, MD 20771

e-mail: [richard@xray-5.gsfc.nasa.gov](mailto:richard@xray-5.gsfc.nasa.gov)

To appear in *The Astrophysical Journal*, vol. 537, July 10, 2000

**ABSTRACT**

We present the results of hard-X-ray observations of four broad-line radio galaxies (BLRGs) with the *Rossi X-Ray Timing Explorer (RXTE)*. The original motivation behind the observations was to search for systematic differences between the BLRGs and their radio-quiet counterparts, the Seyfert galaxies. We do, indeed, find that the Fe K $\alpha$  lines and Compton “reflection” components, which are hallmarks of the X-ray spectra of Seyferts galaxies, are weaker in BLRGs by about a factor of 2. This observational result is in agreement with the conclusions of other recent studies of these objects. We examine several possible explanations for this systematic difference, including beaming of the primary X-rays away from the accretion disk, a low iron abundance, a small solid angle subtended by the disk to the primary X-ray source, and dilution of the observed spectrum by beamed X-rays from the jet. We find that a small solid angle subtended by the disk to the primary X-ray source is a viable and appealing explanation, while all others suffer from drawbacks. We interpret this as an indication of a difference in the inner accretion disk structure between Seyfert galaxies and BLRGs, namely that the inner accretion disks of BLRGs have the form of an ion-supported torus or an advection-dominated accretion flow, which irradiates the geometrically thin outer disk.

## 1. Introduction

An important issue in our study of active galactic nuclei (hereafter AGNs) is the as yet unexplained difference between radio loud and radio-quiet objects. All AGNs are thought to be powered by accretion of matter onto a supermassive black hole, presumably via an equatorial accretion disk. From a theoretical perspective, the accretion disk is an essential ingredient for the formation of radio jets, although the exact mechanism is not well known (see the review by Livio 1996). The observational evidence<sup>1</sup> suggests that both radio-loud and radio-quiet AGNs harbor accretion disks, but it is a mystery why well-collimated, powerful, relativistic radio jets only exist in the former class of object. The origin of the difference could lie in the nature of the host galaxy. At low redshifts ( $z < 0.5$ ) radio-loud AGNs are found only in elliptical galaxies, whereas radio-quiet AGNs can have either elliptical or spiral hosts (Smith et al. 1986; Hutchings, Janson, & Neff 1989; Véron-Cetty & Woltjer 1990; Dunlop et al. 1993; Bahcall et al. 1997; Boyce et al. 1998). This observational trend has led to the suggestion that the interstellar medium of the host galaxy may play an important role in the propagation and collimation of the radio jets on large scales (e.g., Blandford & Levinson 1995; Fabian & Rees 1995). Alternatively, one may seek the fundamental cause of the difference between radio-loud and radio-quiet AGNs in the properties of their accretion flows or the properties of their central black holes. One possibility is that radio-loud AGNs may harbor rapidly spinning black holes, whose energy is extracted electromagnetically via the Blandford & Znajek (1977) mechanism and used to power the radio jets. Rapidly spinning black holes could be associated with elliptical galaxies if both the black hole and the host galaxy result from the merger of two parent galaxies, each with its own nuclear black hole (see Wilson & Colbert 1995). Another possibility is that the inner accretion disks of radio-quiet AGNs are geometrically thin and optically thick throughout (Shakura & Sunyaev 1973) while the inner accretion disks of radio-loud AGNs are ion-supported tori (Rees et al. 1982; known today as advection-dominated accretion flows, or ADAFs, after the work of Narayan & Yi 1994, 1995). Because ADAFs are nearly spherical and parts of the flow are unbound, they can lead to the formation of outflows (e.g., Blandford & Begelman 1999). In either of the above pictures, an additional mechanism may be necessary to *collimate* the radio jets (see for example, Blandford & Payne 1982; Meier 1999).

If the difference between radio-loud and radio-quiet AGNs is related to differences in their central engines, it would lead to observable differences in their respective X-ray spectra, in particular in the properties (profiles and equivalent width) of the Fe K $\alpha$  lines and in the shape of the continuum. This is because the Fe K $\alpha$  lines are thought to result from fluorescence of the dense gas in the geometrically thin and optically thick regions of the disk (e.g., George & Fabian 1991; Matt et al 1992). Similarly, the continuum above 10 keV is thought to include a significant contribution from X-ray photons from the “primary” X-ray source, near the center of the disk, which

---

<sup>1</sup>The most direct observational evidence for the presence of accretion disks in AGNs takes the form of Fe K $\alpha$  lines with disk-like profiles in the X-ray spectra of Seyfert galaxies (e.g., Tanaka et al. 1995; Nandra et al. 1997b) and double-peaked H $\alpha$  lines in the optical spectra of BLRGs (Eracleous & Halpern 1994).

undergo Compton scattering (“reflection”) in the same regions of the disk where the Fe K $\alpha$  line is produced (e.g., Lightman & White 1988; George & Fabian 1991; Matt, Perola, & Piro 1991). It is, therefore, extremely interesting that studies of the X-ray spectra of broad-line radio galaxies (BLRGs) by Zdziarski et al. (1995) and Woźniak et al. (1998) found them to be systematically different from those of (radio-quiet) Seyfert galaxies. In particular, these authors found that the signature of Compton reflection, which is very prominent in the spectra of Seyfert galaxies above 10 keV (Pounds et al. 1989; Nandra & Pounds 1994), is weak or absent in the spectra of BLRGs. Moreover, Woźniak et al. (1997) found that the Fe K $\alpha$  lines of BLRGs are narrower and weaker than those of Seyfert galaxies.

Motivated by the above theoretical considerations and observational results, we have undertaken a systematic study of the X-ray spectra of radio-loud AGNs with *ASCA* and *RXTE* in order to characterize their properties. Our main goal is to compare their spectroscopic properties with those of Seyfert galaxies and test the above ideas for the origin of the difference between the two classes. In our re-analysis of archival *ASCA* spectra of BLRGs and radio-loud quasars (Sambruna, Eracleous, & Mushotzky 1999) we found that the Fe K $\alpha$  lines of some objects are indeed weaker and narrower than those of Seyferts, in agreement with the findings of Woźniak et al. (1997). In other objects, however, the uncertainties are large enough that we cannot reach firm conclusions, thus we have not been able to confirm this result in general. In this paper we present the results of new observations of four BLRGs with *RXTE*, aimed at measuring the shape of their hard X-ray continuum and the equivalent width of their Fe K $\alpha$  lines. As such, these observations complement our study of the *ASCA* spectra of these objects. In §2 we describe the observations and data screening. In §3 we present and discuss the light curves and in §4 we compare the observed spectra with models. In §5 we discuss the implications of the results, while in §6 we summarize our conclusions. Throughout this paper we assume a Hubble constant of  $H_0 = 50 \text{ km s}^{-1} \text{ Mpc}^{-1}$  and a deceleration parameter of  $q_0 = 0.5$ .

## 2. Targets, Observations, and Data Screening

Our targets were selected to be among the X-ray brightest BLRGs, since the background in the *RXTE* instruments is rather high. They are listed in Table 1 along with their basic properties, namely the redshift, the inferred inclination of the radio jet (see Eracleous & Halpern 1998a and references therein), and two different estimates of the column density in the Galactic interstellar medium. The 2–10 keV fluxes are about a few  $\times 10^{-11} \text{ erg s}^{-1} \text{ cm}^{-2}$ , which makes the targets readily detectable by the *RXTE* instruments. The observations were carried out with the Proportional Counter Array (PCA; Jahoda et al. 1996) and the High-Energy X-Ray Timing Experiment (HEXTE; Rothschild et al. 1998) on *RXTE*. Three out of the four objects in our collection (3C 111, Pictor A, and 3C 382) were observed in the spring of 1997 as part of our own guest-observer programs. The fourth object (3C 120) was observed in 1998 February as part of a different program and the data were made public immediately. Although a fair number of observations of 3C 120

Table 1. Target Objects, Basic Properties, and Observation Log

Object	$z$	$i$ <sup>a</sup>	$N_{\text{H}}$ (cm $^{-2}$ )		Observation Start Time (UT)	Duration (hours)
			Galactic <sup>b</sup>	<i>ASCA</i> <sup>c</sup>		
3C 111	0.048	$37^{\circ} > i > 24^{\circ}$	$1.2 \times 10^{22}$	$9.63 \times 10^{21}$	1997/3/22 01:23	62
3C 120	0.033	$14^{\circ} > i > 1^{\circ}$	$1.2 \times 10^{21}$	$1.65 \times 10^{21}$	1998/2/13 04:53	58
Pictor A	0.035	$i > 24^{\circ}$	$4.2 \times 10^{20}$	$8.30 \times 10^{20}$	1997/5/08 02:21	82
3C 382	0.057	$i > 15^{\circ}$	$6.7 \times 10^{20}$	$6.70 \times 10^{20}$	1997/3/28 23:26	47

<sup>a</sup> The inclination angle of the radio jet (see Eracleous & Halpern 1998, and references therein).

<sup>b</sup> The Galactic equivalent H I column density. *References:* 3C 111: Bania, Marscher, & Barvainis (1991); 3C 120: Elvis et al. (1989); Pictor A: Heiles & Cleary (1979); 3C 382: Murphy et al. (1996).

<sup>c</sup> The Galactic equivalent H I column density as measured by the *ASCA* SIS (taken from Sambuona et al. 1999).

Table 2. Exposure Times and Count Rates

Object	PCA (2.5–30 keV)			HEXTE cluster 0 (20-100 keV)		
	Exp. Time	Source Count Rate (s $^{-1}$ PCU $^{-1}$ )	Backg. Count Rate (s $^{-1}$ PCU $^{-1}$ )	Exp. Time	Source Count Rate (s $^{-1}$ )	Backg. Count Rate (s $^{-1}$ )
	(s)	(s $^{-1}$ PCU $^{-1}$ )	(s $^{-1}$ PCU $^{-1}$ )	(s)	(s $^{-1}$ )	(s $^{-1}$ )
3C 111	33,440	22.9	39.1	12,748	7.5	158.4
3C 120	55,904 <sup>a</sup>	25.2	39.9	17,572	3.7	187.5
Pictor A	30,240 <sup>a</sup>	9.6	38.7	12,461	9.4	166.9
3C 382	28,192	13.9	22.0	10,606	3.0	114.9

<sup>a</sup> The PCA exposure time refers to PCUs 0, 1, and 2. PCUs 3 and 4 were off during part of the observation.

exist in the *RXTE* archive, only the above observation was a long, continuous observation suitable for our purposes. All other observations were intended to monitor the variability of this object; they consist of short snapshots spanning a long temporal baseline. Similarly, the only observations of 3C 390.3 available in the archive are also monitoring observations of this type. Therefore we have not included 3C 390.3 in our sample. A log of the observations is included in Table 2. All of the observations fall within PCA gain epoch 3.

The PCA data were screened to exclude events recorded when the pointing offset was greater than  $0^\circ.02$ , when the Earth elevation angle was less than  $10^\circ$ , or when the electron rate was greater than 0.1. Events recorded within 30 minutes of passage though the South-Atlantic Anomaly were also excluded. After screening, time-averaged spectra were extracted by accumulating events recorded in the top layer of each Proportional Counter Unit (PCU) since these include about 90% of the source photons and only about 50% of the internal instrument background. In the case of 3C 111 and 3C 382 we extracted light curves and spectra from all five PCUs. In the case of 3C 120 and Pictor A, PCUs 3 and 4 were turned off part of the time, therefore the spectra from these two PCUs and PCUs 0, 1, and 2 were accumulated separately and then added together. Light curves corresponding to the energy range 3.6–11.6 keV (PCA channels 6–27), were also extracted for all objects and rectified over the time intervals when one or more of the PCUs were not turned on. The PCA background spectrum and light curve were determined using the `L7_240` model developed at the *RXTE* Guest-Observer Facility (GOF) and implemented by the program `pcabackest v.2.1b`. This model is appropriate for “faint” sources, i.e., those producing count rates less than  $40 \text{ s}^{-1} \text{ PCU}^{-1}$ . All of the above tasks were carried out using the `FTOOLS v.4.2` software package and with the help of the `rex` script provided by the *RXTE* GOF, which also produces response matrices and effective area curves appropriate for the time of the observation. The net exposure times after data screening, as well as the total source and background count rates, are given in Table 2.

The HEXTE data were also screened to exclude events recorded when the pointing offset was greater than  $0^\circ.02$ , when the Earth elevation angle was less than  $10^\circ$ . The background in the two HEXTE clusters is measured during each observation by rocking the instrument slowly on and off source. Therefore, source and background photons are included in the same data set and are separated into source and background spectra according to the time they were recorded. After screening we extracted source and background spectra from each of the two HEXTE clusters and corrected them for the dead-time effect, which can be significant because of the high background rate. As with the PCA data, the HEXTE data were screened and reduced using the `FTOOLS v.4.2` software package. The exposure times and count rates in HEXTE/cluster 0 are given in Table 2 for reference. In Figure 1 we show the on-source and background spectra from the PCA and HEXTE/cluster 0, using 3C 111 as an example. This figure illustrates that the background makes the dominant contribution to the HEXTE count rate. In the case of the PCA, the background contributes approximately the same count rate as the source, and its relative contribution increases with energy. At energies above 30 keV the background dominates the count rate in the PCA.

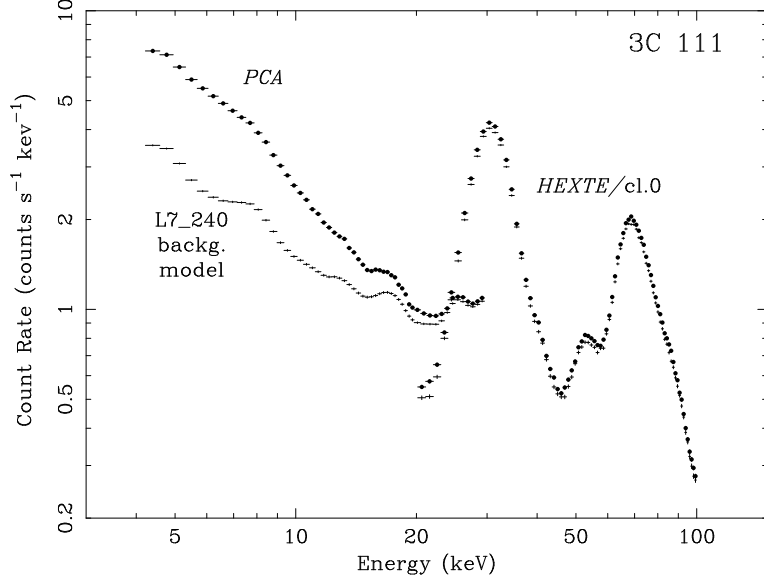


Fig. 1.— The PCA and HEXTE count rate spectra of 3C 111 as examples of typical data obtained from the *RXTE* instruments. The on-source spectrum, shown as large dots, is compared to the background spectrum. In the case of the PCA, the background spectrum was computed using the L7\_240 model, while in the case of the HEXTE the background spectrum was measured during the observation by rocking the instrument on and off source. Notice that the contribution of the background to the total count rate in the PCA increases with energy so that above 30 keV the observed count rate is dominated by the background. In the case of HEXTE, the background dominates the total count rate at all energies.

### 3. Light Curves and Time Variability

In Figure 2 we show the light curves of the four targets. For each object we plot the net count rate (after background subtraction) as well as the the background count rate *vs* time, for reference. The *mean* background count rate is generally comparable to the net source count rate, although the background level varies dramatically over the course of an observation. A visual inspection of the object light curves shows no obviously significant variability. To quantify this result we searched the light curves for variability using two complementary methods:

1. We compared the variance (i.e., the r.m.s. dispersion about the mean) with the average uncertainty of points in the light curve. This method is sensitive to fluctuations in the count rate that exceed the noise level on time scales comparable to the width of the bins in the light curve (the bin width in the light curves of Figure 2 is 640 s). We found no large fluctuations in any of the light curves, save for two instances of poor background subtraction (in Pictor A and 3C 382). We have also computed the “excess variance”,  $\sigma_{\text{rms}}^2$ , following Nandra et al. (1997a), with the following results:  $(3.1 \pm 0.1) \times 10^{-4} \text{ s}^{-2}$  for 3C 111,  $(1.23 \pm 0.01) \times 10^{-3} \text{ s}^{-2}$  for 3C 120,  $(-8.3 \pm 0.6) \times 10^{-4} \text{ s}^{-2}$  for Pictor A, and  $(6.1 \pm 0.4) \times 10^{-4} \text{ s}^{-2}$  for 3C 382. Since their luminosities are  $L_x(2-10 \text{ keV}) \sim 10^{44} \text{ erg s}^{-1}$ , these objects fall on the extrapolation of

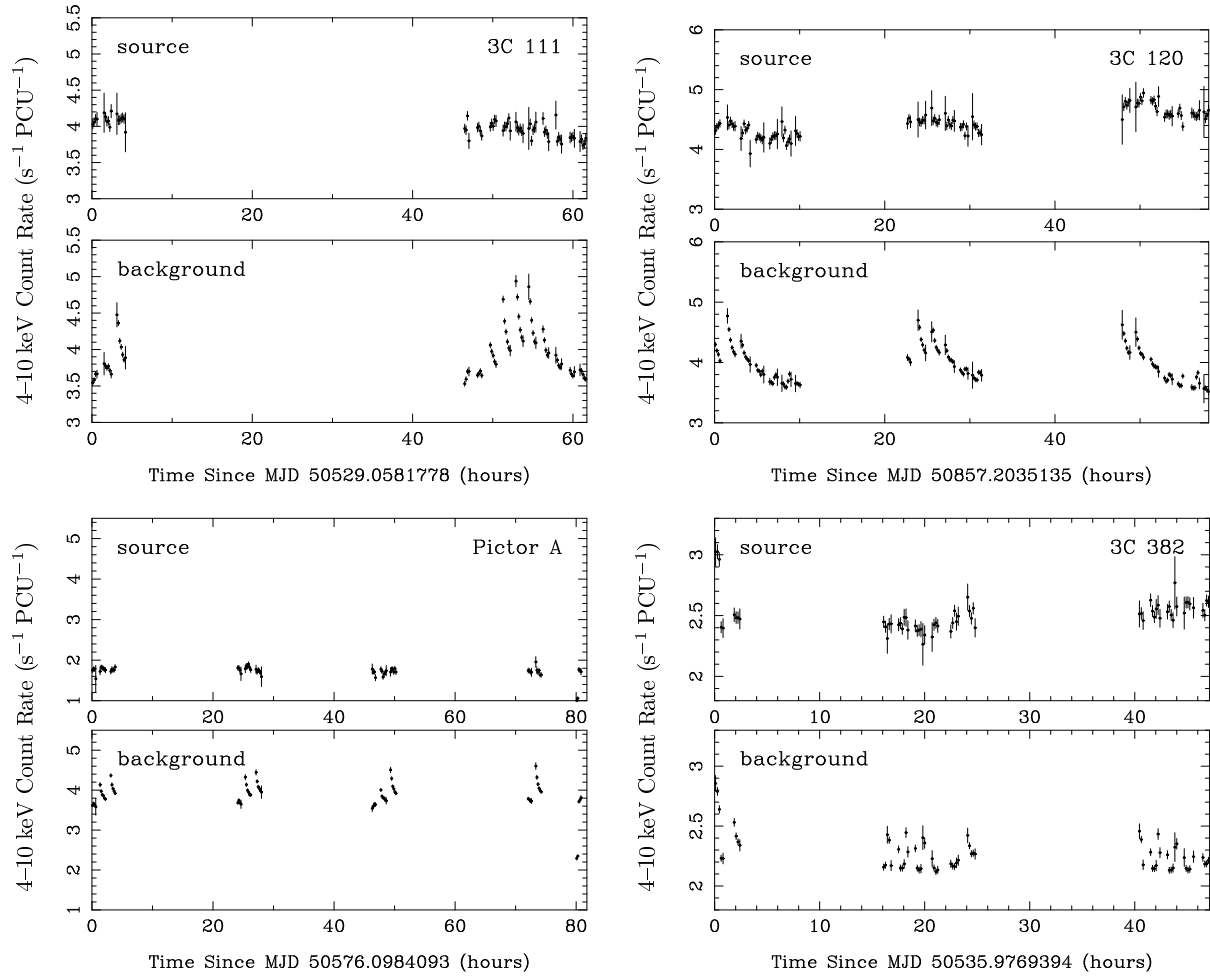


Fig. 2.— Light curves showing the 4–10 keV count rate per PCU of the target BLRGs as a function of time over the course of the *RXTE* observation. For each object we plot the net source light curve and the background light curve computed from the L7\_240 model for reference

the  $\sigma_{\text{rms}}^2 - L_x$  trend for Seyfert galaxies, found by Nandra et al. (1997a). It is noteworthy, however, that the excess variance is small enough at this luminosity that it is comparable to that of LINERs and other very low-luminosity AGNs (Ptak et al. 1998).

2. We fitted each light curve with a polynomial to find the lowest order that gives an acceptable fit. This method detects small, relatively slow variations in the light curve on time scales somewhat shorter than the length of the observations. We found that 3C 111, Pictor A, and 3C 382 show small secular variations on the order of a few percent relative to the mean while 3C 120 shows relatively slow variations with excursions of  $\pm 6\%$  from the mean. For reference, we note that previous observations of 3C 120 with *ASCA* have shown it to be variable at the 20% level (Grandi et al. 1997).

The above results are not surprising since BLRGs are generally known not to be highly variable on short time scales, although they can vary substantially on time scales of several days (see for example the soft X-ray light curve of 3C 390.3 presented by Leighly & O'Brien 1997). We will return to the issue of variability in our later discussion of our overall findings.

#### 4. Model Fits to the Observed Spectra

##### 4.1. The Continuum Shape

The shape of the continuum was determined by fitting models to the observed spectra with the help of the **XSPEC v.10.0** software package (Arnaud 1996). We used PCA response matrices and effective area curves created specifically for the individual observations by the program **pcarsp v.2.37**, taking into account the evolution of the detector properties. All the spectra from individual PCUs were added together and the individual response matrices and effective area were combined accordingly. In fitting the HEXTE spectra we used the response matrices and effective area curves created on 1997 March 20. The spectra from the two HEXTE clusters were not combined. All spectra were rebinned so that each bin contained enough counts for the  $\chi^2$  test to be valid. The PCA spectra were truncated at low energies at 4 keV and at high energies at either 20 or 30 keV depending on the signal-to-noise ratio. In the case of the HEXTE spectra we retained the energy channels between 20 and 100 keV.

We compared the spectra with models consisting of a continuum component and a Gaussian line, modified by interstellar photoelectric absorption. We adopted the absorbing column densities measured by *ASCA* (listed in Table 1), which we held fixed throughout the fitting process. These column densities are comparable to or greater than the Galactic column densities inferred from H I 21 cm observations (see Table 1). The photoelectric absorption cross-sections used were those of Morrison & McCammon (1983). We tried three different models for the continuum shape: a simple power law, a broken power law, and a power law plus its Compton reflection from dense, neutral matter. The Compton reflection model is meant to describe the effects of Compton scattering of

photons from an X-ray source associated with the inner parts of the accretion disk in the gas that makes up the disk proper (e.g., Lightman & White 1988; George & Fabian 1991). The spectrum of reflected X-rays was computed as a function of disk inclination using the transfer functions of Magdziarz & Zdziarski (1995)<sup>2</sup>. The free parameters of this model, in addition to the spectral index of the primary power law and the inclination angle of the disk, are the folding (i.e., upper cut-off) energy of the primary X-ray spectrum, the solid angle subtended by the disk to the central X-ray source, and the abundances of iron and other heavy elements. In our fits the inclination angles were constrained to lie within the limits inferred from the radio properties of each object (see Table 1), and the folding energy of the primary X-ray spectrum was constrained to be greater than 100 keV since all objects are detected by HEXTE up to that energy. The broken power law model is effectively a parameterization of the Compton reflection model: we included it in our suite of continuum models because it serves as an additional verification of the possible departure of the continuum shape from a simple power law. Although the broken power law and Compton reflection models have different shapes in detail, the difference is not discernible at the signal-to-noise ratio of the available HEXTE spectra.

The results of fitting the above models to the observed spectra are summarized in Table 3. The fits yield 2–10 keV unabsorbed fluxes for the target objects in the range  $2\text{--}6 \times 10^{-11}$  erg cm $^{-2}$  s $^{-1}$  and corresponding luminosities in the range  $1\text{--}5 \times 10^{44}$  erg s $^{-1}$ , as listed in Table 3. Spectra with models superposed, are shown in Figures 3 and 4. We find that the spectra of two objects, 3C 111 and Pictor A, are described quite well by a simple power law throughout the observed energy range (4–100 keV), as shown in Figure 3. A broken power law model produces a slightly better fit but the improvement is not statistically significant in view of the additional free parameters (the F-test gives chance improvement probabilities of 0.35 and 0.29 respectively). Similarly, the Compton reflection model does not produce a significantly improved fit either.<sup>3</sup> In the case of the other two objects, 3C 120 and 3C 382, we find that a simple power law does not provide an adequate description of the continuum shape (see Figure 3); a broken power law or a Compton reflection model is required by the data (the F-test gives chance improvement probabilities for the Compton reflection model of  $5 \times 10^{-5}$  and  $5 \times 10^{-3}$ , respectively). Fits of power-law plus Compton reflection models to the spectra of these two objects are shown in Figure 4. Finally, we note that all of the BLRGs in our collection were also observed with *SAX* and detected at high energies up to 50 keV (Padovani et al. 1999; Grandi et al. 1999a,b). The *SAX* spectra yield very similar results to what we obtain here, namely very similar spectral indices and Compton reflection strengths.

---

<sup>2</sup>The Compton reflection calculation is carried out by the `pexrav` model routine in `XSPEC`

<sup>3</sup>In fact, the Compton reflection fit results in a higher value of  $\chi^2$  than the broken power law, even though it has more free parameters.

Table 3. Results of Model Fits<sup>a</sup>

Model and Parameters	3C 111	3C 120	Pictor A	3C 382
CONTINUUM MODELS				
<i>Simple Power Law</i>				
Spectral Index, $\Gamma$	$1.76 \pm 0.01$	$1.82 \pm 0.01$	$1.80 \pm 0.03$	$1.81 \pm 0.02$
Flux density at 1 keV ( $\mu\text{Jy}$ ) <sup>b</sup>	$8.9 \pm 0.2$	$10.6 \pm 0.2$	$3.9 \pm 0.3$	$5.6 \pm 0.2$
Total and Reduced $\chi^2$	52.30, 0.84	125.5, 2.02	38.51, 0.79	68.83, 1.41
<i>Broken Power Law</i>				
Low-Energy Spectral Index, $\Gamma_1$	$1.77 \pm 0.02$	$1.87^{+0.05}_{-0.02}$	$1.77^{+0.04}_{-0.05}$	$1.86^{+0.03}_{-0.04}$
High-Energy Spectral Index, $\Gamma_2$	$1.7 \pm 0.1$	$1.7 \pm 0.1$	$2 \pm 1$	$1.5^{+0.1}_{-0.2}$
Break Energy (keV)	$11 \pm 5$	$9 \pm 1$	$11 \pm 3$	$10 \pm 2$
Flux density at 1 keV ( $\mu\text{Jy}$ ) <sup>b</sup>	$9.0 \pm 0.2$	$11.5 \pm 0.2$	$3.8 \pm 0.3$	$6.1 \pm 0.2$
Total and Reduced $\chi^2$	47.79, 0.80	58.55, 0.98	33.53, 0.71	40.81, 0.73
<i>Power Law + Compton Reflection<sup>c</sup></i>				
Spectral Index, $\Gamma$	$1.78^{+0.03}_{-0.05}$	$1.90 \pm 0.03$	$1.72^{+0.04}_{-0.03}$	$1.92^{+0.07}_{-0.09}$
Folding Energy (keV) <sup>d</sup>	1000 ( $> 100$ )	15,700 ( $> 300$ )	$> 100$	300 ( $> 100$ )
Reflector Solid Angle, $\Omega/2\pi$	$0.1^{+0.4}_{-0.1}$	$0.4^{+0.4}_{-0.1}$	$< 0.3$	$0.5^{+0.8}_{-0.2}$
Inclination Angle, $i$ <sup>e</sup>	$24^\circ$	$10^\circ$	$60^\circ$	$16^\circ$
Flux density at 1 keV ( $\mu\text{Jy}$ ) <sup>b</sup>	$9.1 \pm 0.2$	$11.8 \pm 0.2$	$3.3 \pm 0.2$	$6.5 \pm 0.2$
Total and Reduced $\chi^2$	47.75, 0.81	64.37, 1.09	35.61, 0.76	40.46, 0.88
2–10 keV Flux ( $\text{erg s}^{-1} \text{cm}^{-2}$ ) <sup>f</sup>	$5.6 \times 10^{-11}$	$6.1 \times 10^{-11}$	$2.3 \times 10^{-11}$	$3.3 \times 10^{-11}$
2–10 keV Luminosity ( $\text{erg s}^{-1}$ ) <sup>f</sup>	$5.5 \times 10^{44}$	$2.9 \times 10^{44}$	$1.2 \times 10^{44}$	$4.6 \times 10^{44}$

Table 3—Continued

Model and Parameters	3C 111	3C 120	Pictor A	3C 382
GAUSSIAN EMISSION-LINE MODEL				
Rest Energy Dispersion, $\sigma_{\text{rest}}$ (keV)	< 0.9	< 1.2	< 1.5	< 1.2
FWHM (km s <sup>-1</sup> )	< 44,000	< 55,000	< 70,000	< 56,000
Line Flux (10 <sup>-5</sup> photons s <sup>-1</sup> cm <sup>-2</sup> )	3.2 <sup>+1.1</sup> <sub>-0.5</sub>	4.9 <sup>+1.6</sup> <sub>-1.1</sub>	1.8 ± 0.8	3.1 ± 0.9
Rest Equivalent Width (eV)	60 <sup>+20</sup> <sub>-10</sub>	90 <sup>+30</sup> <sub>-20</sub>	80 ± 40	90 ± 30

<sup>a</sup> All error bars and limits correspond to the 90% confidence level.

<sup>b</sup> The flux density at 1 keV was derived from the normalization of the PCA spectrum. It is related to the monochromatic photon flux at 1keV via  $f_{\nu} = h E N_{\text{E}}$ , where  $h$  is Planck's constant. If  $N_{\text{E}}$  is measured in photons s<sup>-1</sup> cm<sup>-2</sup> keV<sup>-1</sup>, then  $f_{\nu}(1 \text{ keV}) = 663 N_{\text{E}} \mu\text{Jy}$ .

<sup>c</sup> The results reported here were obtained by keeping the abundances of iron and other heavy elements fixed at the solar value.

<sup>d</sup> Best-fitting value and lower limit to the folding energy.

<sup>e</sup> The inclination angles were restricted to lie in the range given in Table 1. In the case of Pictor A and 3C 382, we assumed conservatively that  $i < 60^{\circ}$ .

<sup>f</sup> The observed 2–10 keV fluxes and luminosities turn out to be the same for all models. The luminosities reported here have been corrected for absorption.

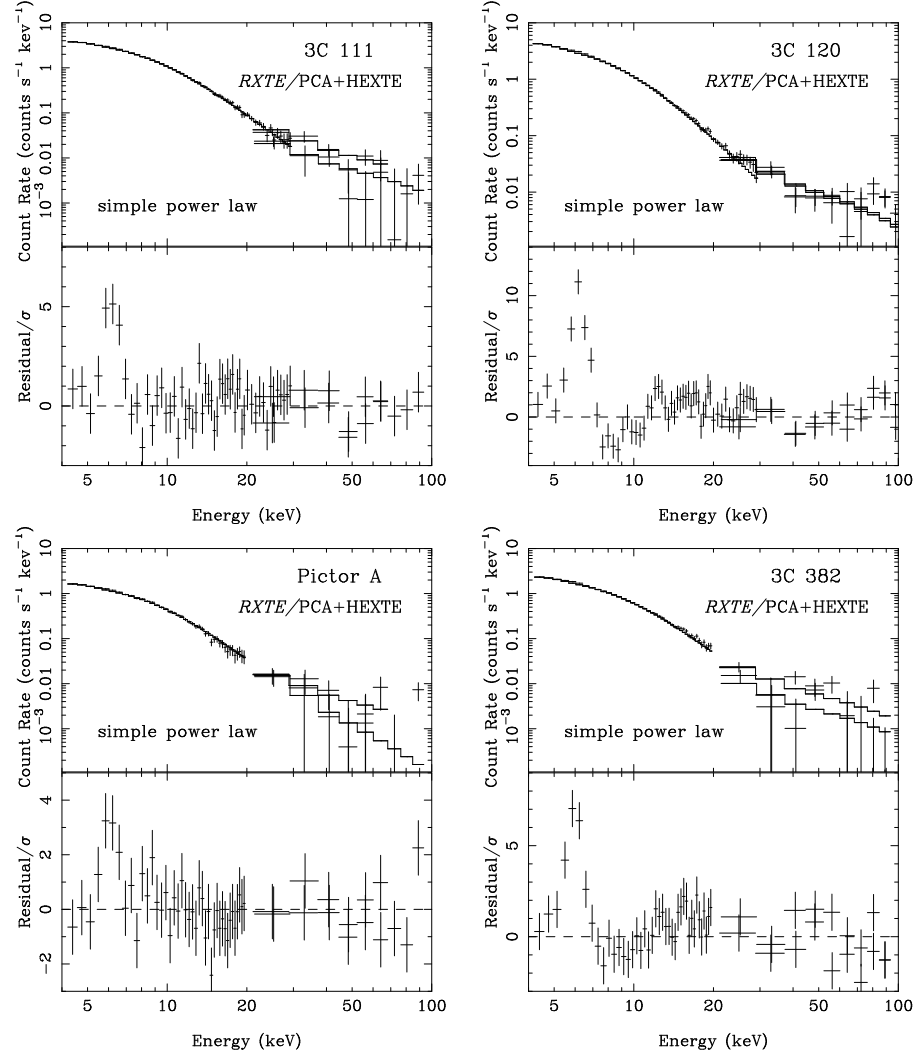


Fig. 3.— The 4–100 keV spectra of the target objects with the best fitting simple power-law continuum model superposed. The model continuum is also modified by interstellar photoelectric absorption. The PCA spectra cover the range 4–30 keV or 4–20 keV (finely binned) while the HEXTE spectra cover the range 20–100 keV (coarsely binned). The lower panel in each set shows the residual spectrum after subtraction of the continuum model, in which the Fe K $\alpha$  line is obvious. The residual count rate at each point has been scaled by the error bar. In the case of 3C 111 and Pictor A, the simple power-law model provides a good description of the continuum. In the case of 3C 120 and 3C 382 however, this model does not provide an adequate description of the continuum: there are substantial negative residuals at energies just below 10 keV and substantial positive residuals at energies between 10 and 20 keV.

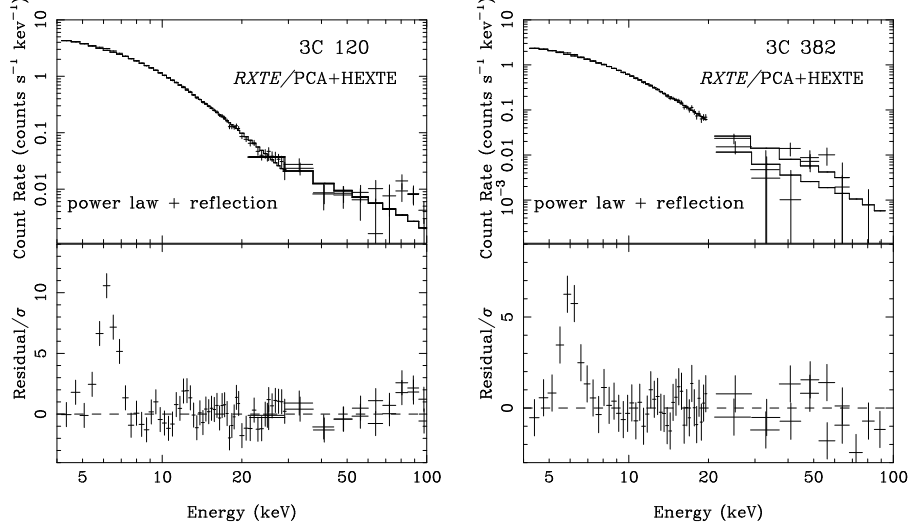


Fig. 4.— The 4–100 keV spectra of 3C 120 and 3C 382 with the best fitting power-law plus Compton reflection model superposed. The model continuum is also modified by interstellar photoelectric absorption. The PCA spectra cover the range 4–30 keV or 4–20 keV (finely binned) while the HEXTE spectra cover the range 20–100 keV (coarsely binned). The lower panel in each set shows the residual spectrum after subtraction of the continuum model, in which the Fe K $\alpha$  line is obvious. The residual count rate at each point has been scaled by the error bar. This model provide a good description of the continuum in these two objects, unlike the simple power-law model shown in Figure 3.

We have explored the multidimensional space defined by the free parameters of the Compton reflection model to find the range of acceptable parameter values. We found that the folding energy of the primary X-ray spectrum is not constrained very well by the observed spectra. Thus our initial physical restriction of  $E_{\text{fold}} > 100$  keV is the only constraint on the folding energy of the primary power-law spectrum. Only in the case of 3C 120 (the brightest object, with the longest exposure time) are we able to derive a somewhat better constraint from the data of  $E_{\text{fold}} > 300$  keV. We are particularly interested in the solid angle subtended by the reflector to the primary X-ray source, which is a diagnostic of the geometry and structure of the accretion flow. This parameter determines the *absolute* strength of the reflected component. In practice, however, it is not straightforward to constrain the reflector solid angle because the inclination angle of the disk and the iron abundance affect the *observed* strength of this component, through projection and photoelectric absorption above the Fe K edge at 7.1 keV (see, for example, George & Fabian 1991; Reynolds, Fabian, & Inoue 1995), respectively. Moreover, the folding energy of the primary X-ray spectrum also affects the determination of the reflector solid angle because it controls the number of energetic photons available for Compton downscattering. We have, therefore, examined the effect of each of the above parameters on our derived values of the reflector solid angle by searching the inclination angle –

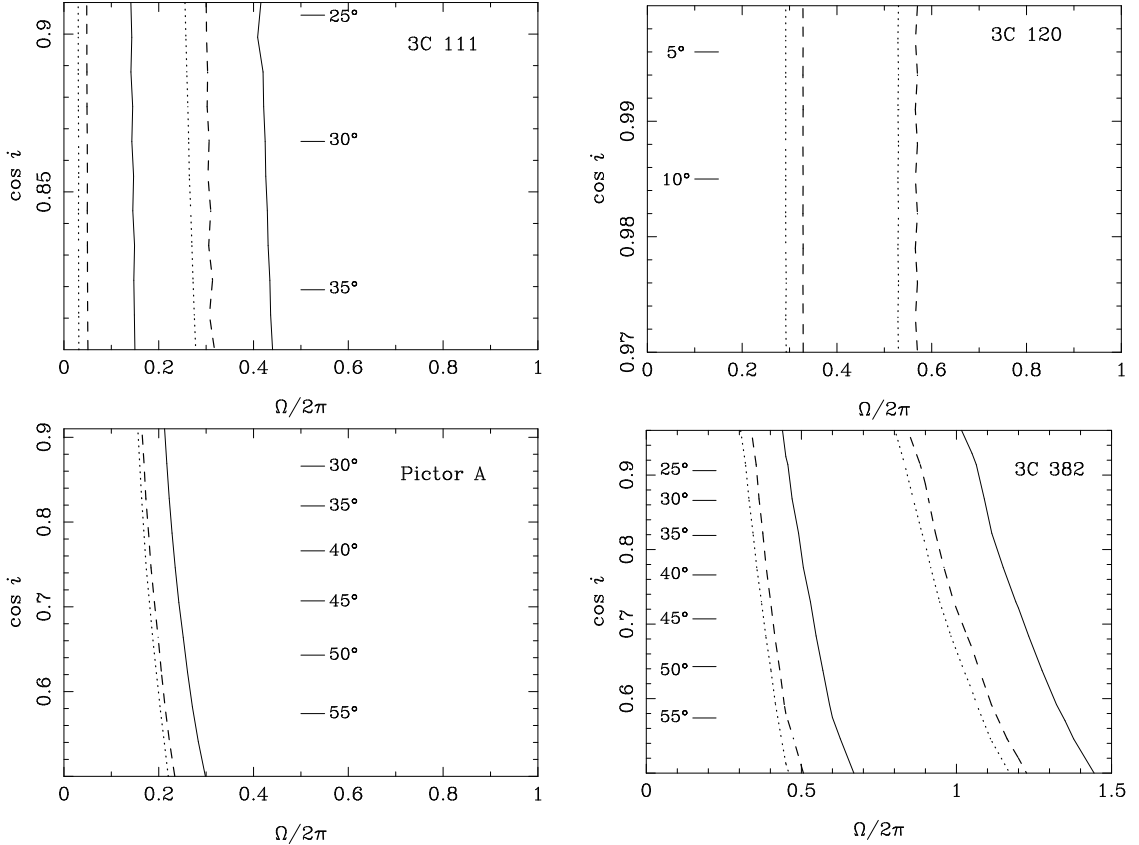


Fig. 5.— 90% confidence contours model in the  $\cos i$ – $\Omega/2\pi$  plane for the Compton reflection. The range of  $\cos i$  plotted on the vertical axis corresponds to the allowed values listed in Table 1. In the cases of Pictor A and 3C 382 we have assumed conservatively that  $i < 60^\circ$ . The region of acceptable fits is bounded by two lines of the same style except for Pictor A, where the lines represent upper limits on  $\Omega/2\pi$ . Different line styles represent different assumed values of the folding energy of the primary power-law spectrum as follows: solid:  $E_{\text{fold}} = 100$  keV, dashed:  $E_{\text{fold}} = 300$  keV, and dotted:  $E_{\text{fold}} = 600$  keV. In the case of 3C 120 the data imply that  $E_{\text{fold}} > 300$  keV, therefore the  $E_{\text{fold}} = 100$  keV contour is not plotted.

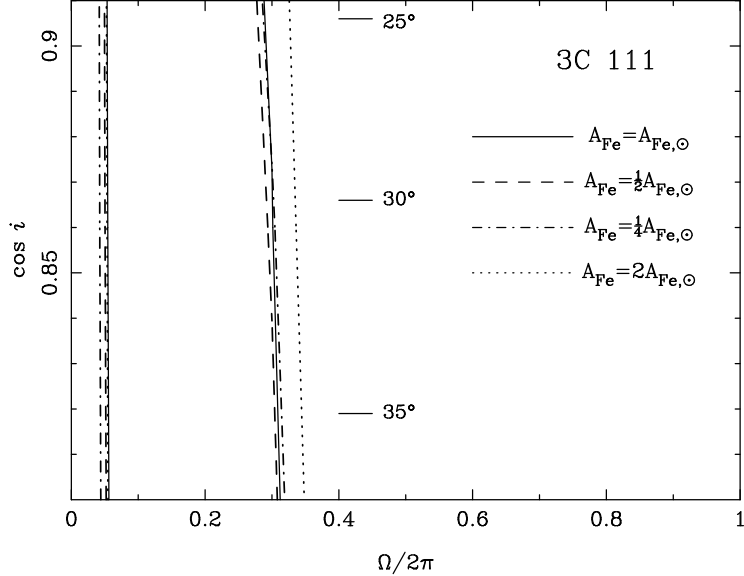


Fig. 6.— An illustration of the negligible effect of the Fe abundance on the confidence contours in the  $\cos i - \Omega/2\pi$  plane, using 3C 111 as an example. The solid lines correspond to a Solar iron abundance, the dashed lines to half Solar, the dash-dot lines to a quarter of Solar, and the dotted lines to twice Solar. The results are nearly identical, independently of the Fe abundance.

solid angle ( $\cos i - \Omega/2\pi$ ) plane for regions with acceptable fits for different assumed values of the folding energy and iron abundance. In other words, we have taken 2-dimensional slices of the 4-dimensional parameter space defined by the solid angle, inclination angle, folding energy, and iron abundance. In Figure 5 we show the 90% confidence contours in the  $\cos i - \Omega/2\pi$  plane for a Solar iron abundance and three different assumed values of the folding energy ( $E_{\text{fold}} = 100, 300$ , and  $600$  keV). The same results are also summarized in Table 3. The strength of the Compton reflection component, as parameterized by  $\Omega/2\pi$  is systematically lower than what is found in Seyferts observed with either *Ginga* or *RXTE*. In particular, we find that  $\Omega/2\pi \lesssim 0.5$ , while in Seyferts  $\Omega/2\pi \approx 0.8$ , with a dispersion of 0.2 (Nandra & Pounds 1994; see also Weaver, Krolik, & Pier 1998 and Lee et al. 1998, 1999 for results from *RXTE* observations). 3C 382 is the only case where the measured value of  $\Omega/2\pi$  is consistent, within uncertainties, with what is found in Seyferts. Pictor A represents the opposite extreme where only an upper limit of  $\Omega/2\pi < 0.3$  can be obtained. In the case of 3C 111, the detection of a Compton reflection hump should be regarded as only marginal since (a) it is only detected at the 90% confidence level and is consistent with zero at the 99% confidence level for  $E_{\text{fold}} = 300, 600$  keV, and (b) the probability of chance improvement of using the Compton-reflection model compared to the power-law model is 0.39 according to the F-test. In the case of 3C 111 and 3C 382 our results are consistent with what Nandra & Pounds (1994) and Woźniak et al. (1998) report based on *Ginga* observations. The iron abundance does not affect the above conclusions at all. We find that the confidence contours in the  $\cos i - \Omega/2\pi$  plane are nearly identical for iron abundances ranging from one quarter to twice the Solar value. We

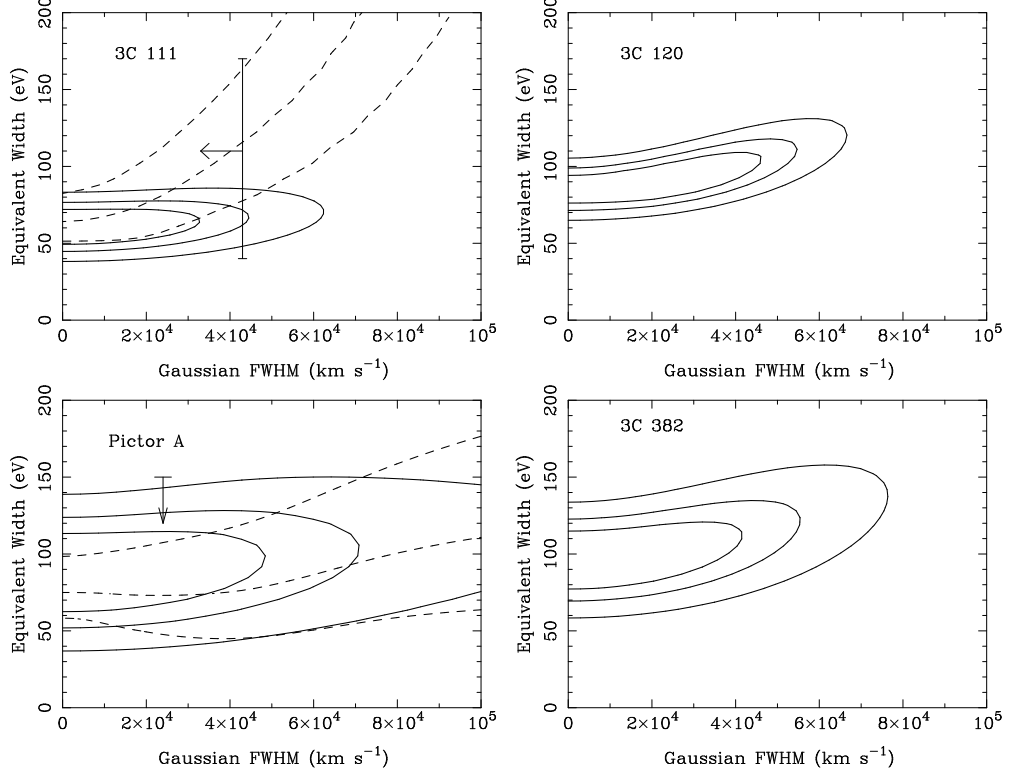


Fig. 7.— 68%, 90%, and 99% confidence contours in the  $EW$ – $FWHM$  plane for the Fe  $K\alpha$  lines. The dashed lines in the case of 3C 111 and Pictor A are the 68%, 90%, and 99% upper limits obtained from *ASCA* spectra by Eracleous & Halpern (1998a,b). The error bar in the 3C 111 plot is the measurement of the line by Reynolds et al. (1998) using *ASCA*, while the upper limit in Pictor A comes from the *SAX* spectrum of Padovani et al. (1999).

illustrate this result in Figure 6 using 3C 111 as an example. This issue is relevant to the strength of the Fe  $K\alpha$  lines whose measurements we report in the next section.

#### 4.2. The Fe $K\alpha$ Line

To study the properties of the Fe  $K\alpha$  line we modeled its profile as a Gaussian of energy dispersion,  $\sigma$ , and intensity,  $I_{FeK\alpha}$ . Because of the low energy resolution of the PCA, more sophisticated models for the line profile are not warranted. For each object we used the best-fitting continuum model and we ignored the HEXTE spectra since they do not extend to energies below 20 keV. After checking that the line centroid energies were consistent with the value for “cold” Fe, we fixed them to the nominal value based on the redshift of each object. We scanned the  $I_{FeK\alpha}$ – $\sigma$  plane for regions where the fit was acceptable, allowing the continuum parameters to vary freely. We found that variations in the continuum parameters were negligible throughout this plane, which

we attribute to the fact that the continuum is well constrained over a wide range of energies. As a result the intensity of the line can be converted to an equivalent width ( $EW$ ) via a simple scaling. We, therefore, present the outcome of the parameter search in the form of confidence contours in the  $EW$ – $FWHM$ <sup>4</sup> plane, which we display in Figure 7. These results are also summarized in Table 3. The lines are unresolved in all cases, with upper limits on the  $FWHM$  ranging from 44,000 to 70,000 km s<sup>−1</sup> (at 90% confidence). The  $EWs$  range from 60 to 90 eV with uncertainties around 30–50% (at 90% confidence).

In the case of 3C 111 and Pictor A, the results obtained here are consistent with the results of *ASCA* and *SAX* observations in which the Fe K $\alpha$  line was either marginally detected (3C 111; Reynolds et al. 1998; Eracleous & Halpern 1998b) or not detected at all (Pictor A; Eracleous & Halpern 1998a; Padovani et al. 1999). In Figure 7 we overlay the *ASCA* upper limits on the *RXTE* confidence contours for reference. In the case of 3C 120 and 3C 382 there is a significant discrepancy between the parameters determined from the *ASCA* spectra and those we determine here: the lines appear to be much broader and much stronger in the *ASCA* spectra than in the *RXTE* spectra. In particular, Grandi et al. (1997) find that the Fe K $\alpha$  line of 3C 120 has  $FWHM = 91,000$  km s<sup>−1</sup> and  $EW = 380$  eV while Reynolds (1997) finds that the Fe K $\alpha$  line of 3C 382 has  $FWHM = 197,000$  km s<sup>−1</sup> and  $EW = 950$  eV. These velocity widths seem uncomfortably large, as pointed out by the authors themselves. In view of the jet inclination angles the line widths imply that some of the line-emitting gas moves faster than light. We suspect that the discrepancy is due to incorrect determination of the continuum in the *ASCA* spectra (see Woźniak et al. 1998 and the discussion by Sambruna et al. 1999). This may be related to the fact that the sensitivity of the *ASCA* SIS, the instrument most commonly used to measure the lines, is extremely low at  $E > 8$  keV. Another possible cause for this discrepancy is calibration uncertainties in the *ASCA* SIS below 1 keV, which affect the detection of a soft excess, hence the determination of the spectral index. In fact, Woźniak et al. (1998) find that if the continuum in the *ASCA* spectra of 3C 120 and 3C 382 is modeled as a broken power law (to account for a soft soft excess) the measured  $FWHM$  and  $EW$  of the Fe K $\alpha$  line become considerably smaller and consistent with our findings. It also noteworthy, however, that Woźniak et al. (1998) have almost certainly underestimated the  $EW$  of the Fe K $\alpha$  line of 3C 120 since they assumed the line to be unresolved. We have also been investigating the cause of this discrepancy through simultaneous *ASCA* and *RXTE* observations of 3C 382, the results of which we will report in a forthcoming paper.

## 5. Discussion

---

<sup>4</sup> $FWHM$  is the full *velocity* width of the line at half maximum.

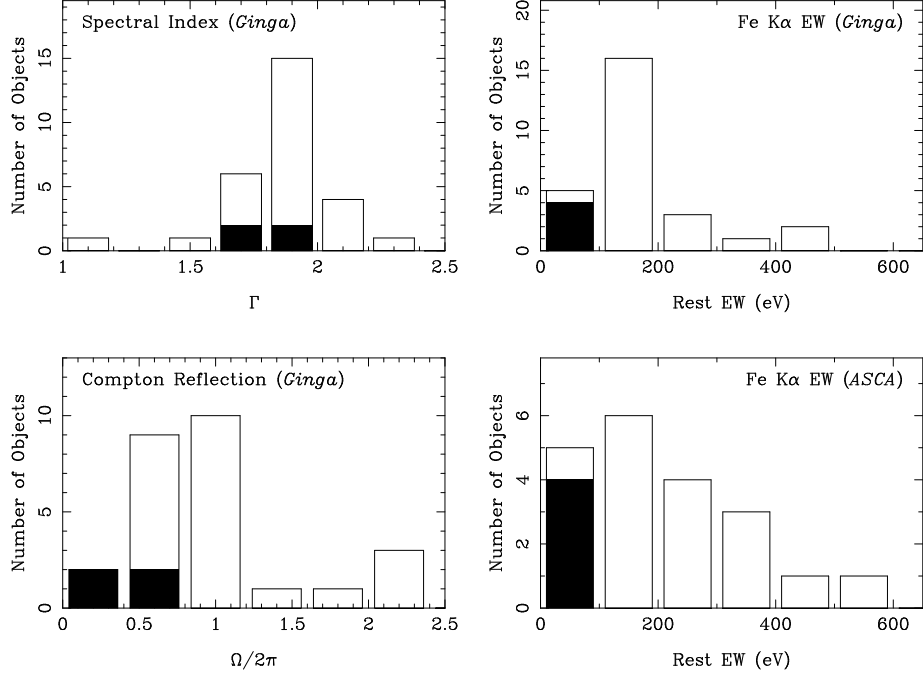


Fig. 8.— The distribution of spectral parameters of Seyfert 1 galaxies observed by *Ginga* (Nandra & Pounds 1994) with the BLRGs observed by *RXTE* marked for comparison. The distribution of *EWs* of Seyfert 1 galaxies observed *ASCA* (Nandra et al. 1997b) is also shown. Seyfert 1 galaxies are represented by hollow bins and BLRGs are represented by filled bins.

### 5.1. Comparison With Seyfert 1 Galaxies

To search for systematic differences between BLRGs and Seyfert 1 galaxies, we compare the X-ray spectral properties of the two classes of objects using the results of our observations. In particular we compare the photon indices, the strength of the Compton reflection hump (parameterized by  $\Omega/2\pi$ ), and the *EW* of the Fe K $\alpha$  line. We use the collection of Seyfert galaxies observed with *Ginga* (Nandra & Pounds 1994) as a comparison sample since the *Ginga* LAC has a broad enough bandpass to allow a measurement of the Compton reflection hump. We also use the collection of Seyfert galaxies observed by *ASCA* (Nandra et al. 1997b) as an additional comparison sample for the *EW* of the Fe K $\alpha$  line since the uncertainties in the determination of the *EW* from the *Ginga* spectra are relatively large. In Figure 8 we show the distribution of the above parameters (spectral index,  $\Omega/2\pi$ , and Fe K $\alpha$  *EW*) among Seyfert 1 galaxies with the values for the 4 BLRGs observed by *RXTE* superposed as filled bins for comparison. A visual inspection of the histograms shows that the spectral indices of BLRGs and Seyfert 1s are fairly similar but the Compton reflection humps and Fe K $\alpha$  lines of BLRGs are considerably weaker than those of Seyfert 1s. Application of the Kolmogorov-Smirnov (KS) test shows that the distributions of Compton-reflection strengths and Fe K $\alpha$  *EWs* are indeed significantly different between Seyferts and BLRGs (chance probabilities of 2% for the former and 4% for the latter; if the *ASCA* *EW* measurements are used instead of the

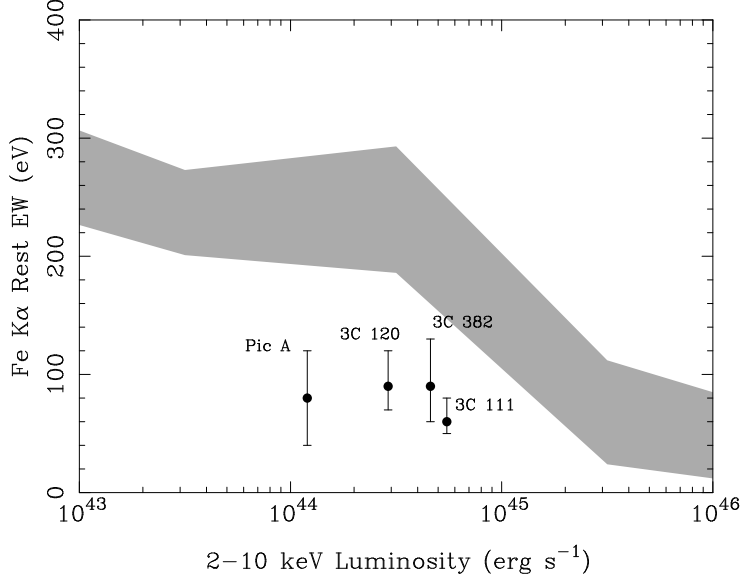


Fig. 9.— The location of the BLRGs observed by *RXTE* in the  $EW-L_X$  plane. The shaded band shows the region occupied by Seyfert 1 galaxies in this plane, according to Nandra et al. (1997c); the width of the band indicates the r.m.s. dispersion above and below the mean  $EW$  in that luminosity bin.

*Ginga* measurements, the chance probability is 3%). In the case of the spectral indices the KS test gives a 41% probability that the spectral indices of Seyferts and BLRGs were drawn from the same parent population. Sambruna et al. (1999) reach a similar conclusion based on the larger sample of BLRGs observed by *ASCA*. To investigate whether the weakness of the Fe K $\alpha$  lines of BLRGs is a consequence of the X-ray Baldwin effect (Nandra et al. 1997c) we also plot the BLRGs observed by *RXTE* in the  $EW-L_X$  diagram shown in Figure 9. This figure shows clearly that the BLRGs have weaker lines than Seyfert 1s of comparable X-ray luminosity, supporting the outcome of the KS test presented above. These results are in agreement with the conclusions of Woźniak et al. (1998) and Sambruna et al. (1999), who found that radio-loud AGNs in general, and BLRGs in particular have weaker Fe K $\alpha$  lines and Compton reflection humps than their radio-quiet counterparts. They are also supported by the results of *SAX* observations by Padovani et al. (1999) and Grandi et al. (1998, 1999). This raises the question of the origin of the observed differences, which we discuss below.

## 5.2. Interpretation

Possible causes of the systematic differences between radio-loud and radio-quiet AGNs were discussed by Woźniak et al. (1998) and by Eracleous & Halpern (1998a). Woźniak et al. (1998) favored a scenario in which the Fe K $\alpha$  is produced in the obscuring torus invoked in the unification schemes for type 1 and type 2 AGNs. A column density in the reprocessing medium of  $N_H \sim 10^{23} \text{ cm}^{-2}$  was found to reproduce the equivalent width of the Fe K $\alpha$  line. In this picture the

reflection hump is still due to Compton scattering in the accretion disk. However the continuum is postulated to be beamed away from the disk so that the illumination of the disk is ineffective with the result that Compton reflection and line emission from the disk made a relatively small contribution to the observed spectrum of BLRGs. Eracleous & Halpern (1998a) concluded that there were two equally viable explanations for the weakness of the Fe  $K\alpha$  line in the *ASCA* spectra of Pictor A and 3C 111: either the iron abundance in BLRGs is low (it need only be lower by a factor of 2 compared to Seyferts), or the solid angle subtended by the reprocessor to the primary X-ray source is about a factor of 2 smaller in BLRGs than in Seyferts. Another possibility worth examining is that the disks of BLRGs are in a higher ionization state than those of Seyfert galaxies. In such a case, photons emerging from the disk will be Compton scattered by electrons in the ionized skin of the disk, with the result that both the Fe  $K\alpha$  line and the Fe K edge are smeared out (Ross, Fabian, & Brandt 1996; Ross, Fabian, & Young 1999) and appear weaker. Finally, we mention one more possible explanation: X-rays with a featureless spectrum from the jets of BLRGs “dilute” the X-ray spectrum from the central engine, which is otherwise similar to that of Seyferts. This possibility was dismissed by both Woźniak et al. (1998) and by Eracleous & Halpern (1998a), but we re-examine it here in the light of the latest observational results. We evaluate the merits and applicability of these scenarios below.

1. *Continuum beamed away from the accretion disk resulting in weak Fe  $K\alpha$  emission and Compton reflection from it; additional Fe  $K\alpha$  emission from obscuring torus:* This explanation requires *mild* beaming by a sub-relativistic outflow, so that the X-ray beam has an opening angle that is just right to illuminate the obscuring torus effectively, while it illuminates the accretion disk only “mildly” so that the strength of the Compton reflection hump from the disk is suppressed. This scenario suffers from the following drawbacks, which make it untenable:
  - (a) It is contrary to observational evidence showing that the jets of BLRGs are highly relativistic. In particular, such jets are thought to have bulk Lorentz factors of  $\gamma = (1 - \beta^2)^{-1/2} \gtrsim 10$  (Padovani & Urry 1992; Ghisellini et al. 1993, 1998), which implies that their emission is tightly focused in a cone of opening angle  $\psi \approx 1/\gamma \lesssim 6^\circ$ . This means that neither the accretion disk nor the obscuring torus can be illuminated by the primary X-ray source, if this is associated with a jet. Postulating that the X-ray continuum is beamed away from the disk without being associated with the jet is an *ad hoc* solution with no clear physical foundation. In fact, Reynolds & Fabian (1997) consider beaming of the X-ray continuum produced in a disk corona and conclude that the beamed emission is directed in large part towards the disk. The result is that the *EW* of the Fe  $K\alpha$  line is *enhanced*.
  - (b) If the accretion disk is responsible for producing a Compton reflection hump, then it should also be producing Fe  $K\alpha$  emission, which should be added to the emission from the obscuring torus. If this were the case, the Fe  $K\alpha$  *EW* should have been disproportionately large compared to the strength of the Compton reflection hump,

since it would include contributions from two different sources. The observations, however, show that both the strength of the Compton reflection hump and the *EW* of the Fe K $\alpha$  line are weaker by about the same factor compared to Seyfert galaxies.

- (c) Part of the motivation of Woźniak et al. (1998) for associating the source of the Fe K $\alpha$  line with the obscuring torus was their claimed lack of correlated variations of the continuum and line intensities in 3C 390.3. This conclusion is not justified by their data, however, because of the large uncertainties in the line intensity: a factor of 2 at 68% confidence (see their Figure 7). Since the continuum variations span a range of a factor of 2, it is next to impossible to find correlated variations in the line intensities when the error bars are as large as they are.

Independently of the above arguments, this interpretation can be tested observationally using the profiles of the Fe K $\alpha$  lines. If the lines are produced in the accretion disk, their profiles should be considerably broader than if they are produced in the obscuring torus, with very distinct asymmetries caused by Doppler and gravitational redshift.

2. *Low Iron Abundance:* A low iron abundance would have a very clear observational consequence: it would make the Fe K $\alpha$  lines weaker but at the same time it would make the Compton reflection humps stronger by reducing the opacity above the Fe K edge (George & Fabian 1991; Reynolds, Fabian, & Inoue 1995). The *RXTE* spectra presented here contradict this interpretation since both the Fe K $\alpha$  lines and the Compton reflection humps are weak. We have specifically tested the hypothesis that the iron abundance is low with negative results (see §4.1 and Figure 6). Based on these findings we conclude that a low iron abundance is not a viable interpretation.
3. *Small solid angle subtended by the reprocessor to the primary X-ray source:* The weakness of both the Fe K $\alpha$  line and the Compton reflection hump can be explained if the reprocessing medium subtends a relatively small solid angle to the primary X-ray source. In the case of Seyfert galaxies, the primary X-ray source is thought to make up a hot corona overlaying the disk proper, which serves as the reprocessor. In such a picture the reprocessor covers half the sky as seen from the primary X-ray source, i.e., the solid angle is  $\Omega/2\pi = 1$ , in reasonable agreement with the observed X-ray spectra of Seyfert galaxies. In the case of BLRGs, on the other hand, the *RXTE* spectra indicate that  $\Omega/2\pi \lesssim 0.5$ . This can be explained in a picture where the primary X-ray source is a quasi-spherical ion torus (or ADAF) occupying the inner disk and the reprocessor is the geometrically thin, optically thick outer disk. The solid angle subtended by the outer disk to the ion torus is  $\Omega/2\pi < 0.5$  on geometrical grounds (Chen & Halpern 1989; Zdziarski, Lubiński & Smith 1999), in agreement with our findings. This is our preferred interpretation over all the others we consider here and has the following additional attractive features: (a) the association of ion tori with BLRGs is appealing because these structures offer a way of producing radio jets as we have mentioned in §1, and (b) such an accretion disk structure also explains the double-peaked profiles of the Balmer lines in some

of these objects (Pictor A, 3C 382, and 3C 390.3; Chen & Halpern 1989; Eracleous & Halpern 1994; Halpern & Eracleous 1994). The profiles of the Fe K $\alpha$  lines offer a way of testing this scenario further: if the lines do indeed originate in the outer parts of the accretion disk at radii  $R \gtrsim 100 R_g$  (where  $R_g \equiv GM/c^2$  is the gravitational radius, with  $M$  the mass of the black hole), then their profiles should be narrower than those observed in Seyfert galaxies, although still skewed, asymmetric, and possibly double-peaked.

4. *Smearing by Compton scattering in an ionized accretion disk:* If the disk is photoionized so that the ionization parameter reaches values of  $\xi > 10^4$ , photons emerging from the disk will be Compton scattered by hot electrons in the disk atmosphere. This process will smear out of the Fe K $\alpha$  line and the Compton reflection and make them appear weaker (see Ross et al. 1996, 1999). We consider this an unlikely explanation for our results because the observed spectra lack the distinct signature of this process. Namely, at  $\xi > 10^3$ , the Fe K $\alpha$  lines is considerably broadened by Compton scattering while at  $\xi > 10^4$ , the line centroid shifts to energies greater than 6.7 keV because most of the iron atoms are highly ionized. Neither of these effects is observed in either the *RXTE* PCA spectra presented here or in published *ASCA* spectra.
5. *Dilution of the X-ray spectrum of the central engine by beamed emission from the jet:* At first glance this is a plausible interpretation since a flux from the jet comparable to the flux from the central engine would provide the necessary dilution. This hypothesis does not withstand close scrutiny, however, for the following reasons: (a) as shown by Woźniak et al. (1998) the spectra of BLRGs *cannot* be described as the sum of two power-law components, which should have been possible if they included comparable contributions from the jet and the central engine, (b) the light curves of our targets (§3 and Figure 2) do not show a great deal of variability on time scales up to a few days, contrary to what is observed in blazars; 3C 120 shows the largest variability amplitude, consistent with the small inclination angle of the jet to the line of sight (Table 1), which make the contribution of the jet to the observed X-ray emission rather significant, (c) the X-ray spectral indices of BLRGs are systematically different from those of blazars, which are typically around 1.4 to 1.5 (Kubo et al. 1998), and (d) 3C 120 is the object where dilution of the observed spectrum by emission from the jet is expected to be most severe because of the very small inclination angle; nevertheless both an Fe K $\alpha$  line and a Compton reflection hump are detected, when they should have been undetectable.

## 6. Conclusions and Future Prospects

Our study of the hard X-ray spectra of 4 BLRGs observed with *RXTE* has shown them to be systematically different from those of Seyfert galaxies. In particular, the Fe K $\alpha$  lines and Compton reflection humps in the spectra of BLRGs are at least a factor of 2 weaker than those observed in the spectra of Seyfert galaxies. This result is consistent with the conclusions of previous studies

and is supported by the results of *SAX* observations of the same targets. After examining several possible explanations for this difference, we conclude that the most likely one is that the solid angle subtended by the source of these spectral features to the primary X-ray source is a factor of 2 smaller in BLRGs than in Seyferts. Since this reprocessing medium is thought to be the accretion disk, we interpret this difference as the result of a difference in the accretion disk structure between BLRGs and Seyferts. More specifically, we argue that if the inner accretion disks of BLRGs have the form of an ion-supported torus (or an ADAF) that irradiates the outer disk, then the observed differences can be explained. We find this explanation particularly appealing because ADAFs offer a possible way of producing the radio jets in these objects and because such a disk structure can also account for the double-peaked Balmer line profiles observed in these objects.

This interpretation, as well as some of the other scenarios we have considered, can be tested further by studying the profiles of the Fe K $\alpha$  lines. Unfortunately, such a test has not been possible so far using spectra from *ASCA*, because of their low signal-to-noise ratio. It will be possible, however, to carry out the test using spectra from upcoming observatories such as *XMM* and *Astro-E*. Correlated variations of the intensity of the Fe K $\alpha$  line and the strength of the X-ray continuum afford an additional observational test of these ideas. The light travel time between the ion torus and the outer accretion disk is  $\tau_\ell \approx 1.7 (R/300 R_g) (M/10^8 M_\odot)$  days, which means that one may expect lags of this order between line and continuum variations. If, on the other hand, the line is produced very close to the center of the disk, the lags should be considerably shorter, while if the line is produced in the obscuring torus, the lags should be on the order of several years. Monitoring campaigns with *RXTE* may provide the data needed for such a test.

We are grateful to Karen Leighly and Niel Brandt for useful discussions and we thank the anonymous referee for thoughtful comments. This work was supported by NASA through grants NAG5-7733 and NAG5-8369. During the early stages of this project M.E. was based at the University of California, Berkeley, and was supported by a Hubble Fellowship (grant HF-01068.01-94A from the Space Telescope Science Institute, which is operated for NASA by the Association of Universities for Research in Astronomy, Inc. under contract NAS 5-2655). R.M.S. also acknowledges support from NASA contract NAS-38252.

## REFERENCES

Arnaud, K. 1996 in *ASP Conf. Ser.* 101, *Astronomical Data Analysis Software and Systems V*, ed. G. Jacoby & J. Barnes (San Francisco: ASP), 17

Bahcall, J. N., Kirhakos, S., Saxe, D. H., & Schneider, D. P. 1997 *ApJ*, 479, 642

Bania, T. M., Marscher, A. P., & Barvainis, R. 1991, *AJ*, 101, 2147

Blandford, R. D. & Begelman, M. C. 1999, *MNRAS*, 303, L1

Blandford, R. D. & Levinson, A. 1995, *ApJ*, 441, 79

Blandford, R. D. & Payne, D. G. 1982, *MNRAS*, 199, 883

Blandford, R. D. & Znajek, R. L. 1977, *MNRAS*, 179, 433

Boyce, P. J. et al. 1998, *MNRAS*, 298, 121

Chen, K. & Halpern, J. P. 1989, *ApJ*, 344, 115

Dunlop, J. S., Taylor, G. L., Hughes, D. H., & Robson, E. I. 1993, *MNRAS*, 264, 455

Elvis, M., Lockman, F. J., Wilkes, B. J. 1989, *AJ*, 97, 777

Eracleous, M. & Halpern, J. P. 1994, *ApJS*, 90, 1

Eracleous, M. & Halpern, J. P. 1998a, *ApJ*, 505, 577

Eracleous, M., & Halpern, J. P. 1998b, in *Accretion Processes in Astrophysical Systems: Some Like It Hot*, eds. S. S. Holt & T. R. Kallman, (New York: AIP), 261

Fabian, A. C. & Rees, M. J. 1995, *MNRAS*, 277, L55

George, I. M. & Fabian, A. C. 1991, *MNRAS*, 249, 352

Ghisellini, G., Celotti, A., Fossati, G., Maraschi, L., & Comastri, A. 1998, *MNRAS*, 301, 451

Ghisellini, G., Padovani, P., Celotti, A., & Maraschi, L. 1993, *ApJ*, 407, 65

Grandi, P. et al. 1999a, in *The Extreme Universe, Proceedings of the 3rd Integral Workshop, Astrophysical Letters and Communications*, in press (astro-ph/9811468)

Grandi, P., Urry, C. M., & Maraschi, L. 1999b in *Life Cycles of Radio Galaxies, Proceedings of STScI International Workshop*, ed. J. Biretta, *New Astronomy Reviews*, in press

Grandi, P., Sambruna, R. M., Maraschi, L., Matt, G., Urry, C. M., & Mushotzky, R. F. 1997, *ApJ*, 487, 636.

Halpern, J. P., & Eracleous, M. 1994, *ApJ*, 433, L17

Heiles, C. & Cleary, M. N. 1979, *Australian J. Phys. Astrophys. Suppl.*, 47, 1

Hutchings, J. B., Janson, T., & Neff, S. G. 1989, *ApJ*, 342, 660

Jahoda, K., Swank, J. H., Giles, A. B., Stark, M. J., Strohmayer, T., Zhang, W., & Morgan, E. H. 1996, in *EUV, X-ray and Gamma-Ray Instrumentation for Astronomy VII*, SPIE Proc., eds. O. Siegmund & M. Gummin, 2808, 59

Kubo, H., Takahashi, T., Madejski, G., Tashiro, M., Makino, F., Inoue, S., & Takahara, F. 1998, *ApJ*, 504, 693

Lee, J. C., Fabian, A. C., Reynolds, C. S., Iwasawa, K., & Brandt, W. N. 1998, *MNRAS*, 300, 583

Lee, J. C., Fabian, A. C., Brandt, W. N., Reynolds, C. S., & Iwasawa, K. 1999, *MNRAS*, in press (astro-ph/9907352)

Leighly, K. M. & O'Brien, P. T. 1997, *ApJ*, 481, L15

Lightman, A. P. & White, T. R. 1988, *ApJ* 335, 57

Livio, M. 1997 in *Accretion Phenomena and related Outflows: IAU Colloquium 163*, eds. D. T. Wickramasinghe, L. Ferrario, & G. V. Bicknell (San Francisco, ASP), 845

Magdziarz, P. & Zdziarski, A. A. 1995, *MNRAS*, 273, 837

Matt, G., Perola, G. C., & Piro, L. 1991, *A&A*, 247, 25

Matt, G., Perola, G. C., Piro, L. & Stella, L. 1992, *A&A*, 257, 63

Meier, D. L. 1999 in *Life Cycles of Radio Galaxies*, Proceedings of STScI International Workshop, ed. J. Biretta, *New Astronomy Reviews*, in press

Morrison, R., & McCammon, D. 1983, *ApJ*, 270, 119

Murphy, E. M., Lockman, F. J., Laor, A., & Elvis, M. 1996, *ApJS*, 105, 369

Nandra, K., George, I. M., Mushotzky, R. F., Turner, T. J., & Yaqoob, T. 1997a, *ApJ*, 476, 70

Nandra, K., George, I. M., Mushotzky, R. F., Turner, T. J., & Yaqoob, T. 1997b, *ApJ*, 477, 602

Nandra, K., George, I. M., Mushotzky, R. F., Turner, T. J., & Yaqoob, T. 1997c, *ApJ*, 488, L91

Nandra, K. & Pounds, K. A. 1994, *MNRAS*, 268, 405

Narayan, R. & Yi, I. 1994, *ApJ*, 428, L13

Narayan, R. & Yi, I. 1995, *ApJ*, 444, 231

Padovani, P., Morganti, R., Siebert, J., Vagnetti, F., & Cimatti, A. 1999, *MNRAS*, 304, 829

Padovani, P., & Urry, C. M. 1992, *ApJ*, 387, 449

Pounds, K. A., Nandra, K., Stewart, G. C., & Leighly, K. 1989, *MNRAS*, 240, 769

Ptak, A. Yaqoob, T., Mushotzky, R., Serlemitsos, P., & Griffiths, R. 1998 *ApJ*, 501, L37

Rees, M. J., Begelman, M. C., Blandford, R. D., & Phinney, E. S. 1982, *Nature*, 295, 17

Reynolds, C. S. 1997, *MNRAS*, 286, 513

Reynolds, C. S., Iwasawa, K., Crawford, C. S., & Fabian, A. C. 1998, *MNRAS*, 299, 410

Reynolds, C. S. & Fabian, A. C. 1997 *MNRAS*, 290, L1

Reynolds, C. S., Fabian, A. C., & Inoue, H. *MNRAS*, 276, 1311

Ross, R. R., Fabian, A. C., & Brandt, W. N. 1996, *MNRAS*, 278, 1082

Ross, R. R., Fabian, A. C., & Young, A. J. 1999, MNRAS, 306, 461

Rothschild, R. et al. 1998, ApJ, 496, 538

Sambruna, R., Eracleous, M., & Mushotzky, R. F. 1999, ApJ, 526, 60

Shakura, N. I. & Sunyaev, R. A. 1973, A&A, 24, 337

Smith, E. P., Heckman, T. M., Bothun, G. D. Romanishin, W., & Balick, B. 1986, ApJ, 306, 64

Tanaka, Y. et al. 1995, Nature, 375, 659

Véron-Cetty, M. P. & Woltjer, L. 1990, A&A, 236, 69

Weaver, K. A., Krolik, J. H., & Pier, E. A. 1998, ApJ, 498, 213

Wilson, A. S. & Colbert, E. J. M. 1995, ApJ, 438, 62

Woźniak, P. R., Zdziarski, A. A., Smith, D., Madejski, G. H., & Johnson, W. N. 1998, MNRAS, 299, 449.

Zdziarski, A. A., Johnson, N. W., Done, C., Smith, D., & McNaron-Brown, K. 1995, ApJ, 438, L63

Zdziarski, A. A., Lubiński, P., & Smith, D. A. 1999, MNRAS, 303, L11